Petroleum Science 18 (2021) 1530–1542

Contents lists available at ScienceDirect

Petroleum Science

journal homepage: www.keaipublishing.com/en/journals/petroleum-science

Original Paper

Improved activity of Ni–Mo/SiO_2 bimetallic catalyst synthesized via sol-gel method for methylcyclohexane cracking

Jun Zhang [a], Ting Chen [a], Yi Jiao [b, *], Mei Cheng [a], Lin-Lin Wang [a], Jian-Li Wang [c, **], Xiang-Yuan Li [a], Yao-Qiang Chen [c]

[a] School of Chemical Engineering, Sichuan University, Chengdu, 610064, Sichuan, China
[b] Institute of New Energy and Low-Carbon Technology, Sichuan University, Chengdu, 610064, Sichuan, China
[c] College of Chemistry, Sichuan University, Chengdu, 610064, Sichuan, China

ARTICLE INFO

Article history:
Received 7 August 2020
Accepted 5 March 2021
Available online 1 September 2021

Edited by Xiu-Qiu Peng

Keywords:
Ni dispersion
Ni–Mo/SiO_2
Catalytic cracking
Citric acid
Sol-gel method
Acidity modulation

ABSTRACT

To improve the cracking behavior of hydrocarbon, Ni–Mo/SiO_2 bimetallic catalysts were synthesized by different preparation methods (sol-gel, co-impregnation and single-impregnation) and added the additives (citric acid, polyethylene glycol and cetyltrimethylammonium bromide) based on the most suitable method above. The cracking reaction of methylcyclohexane under supercritical conditions was performed as the probe reaction to estimate the catalytic performance, and the properties of Ni–Mo/SiO_2 catalyst were characterized by N_2 absorption-desorption, XRD, XPS, H_2-TPR, NH_3-TPD, in-situ IR of NH_3 desorption, HRTEM and STEM-mapping so as to study the structure-activity relationship. The catalyst synthesized via sol-gel method showed the best conversion and heat sink, being 81.8% and 3.81 MJ/kg, which was closely related to strong mutual effect between active components and SiO_2 as well as strong acid sites. Besides, the introduction of additives by sol-gel method has an affirmative influence on properties of Ni–Mo/SiO_2 catalysts, being that the acidity (more L and B acid sites) was modulated and organic groups interact with metal to suppress the aggregation of metal species (Ni and Mo), thereby enhancing the catalytic activity. At 750 °C, the conversion (89.3%) as well as heat sink (3.99 MJ/kg) of MCH cracking obtained an optimum over Ni–Mo/SiO_2 catalyst with addition of citric acid.

1. Introduction

Thermal barrier is an urgent problem affecting the further development of hypersonic vehicle. Endothermic hydrocarbon fuel (EHF) with good heat absorption capacity (physical and chemical heat sink) has been considered as effective coolant because it can practically remove the excess heat from combustion chamber of scramjet engine (Edwards, 2006; Jiao et al., 2014; Qin et al., 2013; Zhu et al., 2018). Physical heat sink is subject to nature of EHF, and chemical heat sink mainly derives from endothermic reactions, such as cracking. Compared with EHF pyrolysis, catalytic cracking of EHF owning higher cracking depth, higher selectivity of special products (hydrogen and olefins) and releasing higher heat sink, has attracted considerable attention (Jiao et al., 2018; Liu et al., 2019; Ye et al., 2019; Zhang et al., 2020). Additionally, methylcyclohexane (MCH), as the simplest alkyl substituted cyclohexane and an important composition of EHF, is of great significance to study the cracking behavior of EHF (Borm et al., 2010; Sim et al., 2020; Wang et al., 2017).

On account of high activity for C–H and C–C bonds of hydrocarbon and low cost, Ni-based catalyst was widespread applied in catalytic cracking (Huang et al., 2016; Pevneva et al., 2019). Ma et al. (2017) reported that cracking of purified bio-oil/ethanol with Ni-based catalyst at 500 °C exhibited yield of 36.8 vol% carbon dioxide and carbon monoxide among the gaseous products. Chin et al. (2006) found that the initial ethane conversion and H_2 selectivity over the Ni/SiO_2 catalyst at 650 °C could reach 100% and 39% respectively, while the pyrolysis of ethane could be neglected. Long et al. (2020) prepared NiO nanoparticles modified ZSM-5 as quasi homogeneous catalyst for cracking *n*-decane (0.43 g/s), presenting heat absorption capacity of 4.59 MJ/kg at 780 °C. From the above, Ni-based catalyst owns high cracking activity. However, carbon

* Corresponding author.
** Corresponding author.
E-mail address: jiaoyiscu@163.com (Y. Jiao).

https://doi.org/10.1016/j.petsci.2021.08.009

deposition and easy sintering under high temperature are two of the most challenging issues. As an inevitable by-product of all hydrocarbon fuels cracking, carbon deposition would cover the active sites of catalytic coating to weaken the promotion effect of catalyst and cause heat transfer deterioration, resulting in experimental failure (blockage), or even security incidents. Meantime, the sintering of Ni species under high temperature would bring about the decrease of active metal sites. These two issues are closely in connection with acidity of catalyst support as well as the properties of Ni species (Qin et al., 2011). Furthermore, the cracking reaction can occur on the strong acid sites, in contrast, both weak and strong acid sites can catalyze the coking reaction so that the appropriate acid sites is good for cracking reaction (Zhang et al., 2020; Lin et al., 2015). At present, numerous researches have been carried out to solve the above problems in the terms of adding modifiers (Han et al., 2020; He et al., 2018; Pevneva et al., 2019; Yu et al., 2014) and tuning preparation methods (Li et al., 2006; Liu et al., 2007). Our previous work (Jiao et al., 2018; Zhang et al., 2017) has revealed that incorporation of molybdenum (Mo) into ZrO_2–TiO_2–Al_2O_3 can give rise to proper acid sites on account of altered electronegativity of support compared with its counterpart promoter (Mn, Fe and W). Behnejad et al. (2019) have synthesized Ni–Mo/γ-alumina catalyst, which presented small active metal size and increase in dispersion of Ni and Mo, leading to produce more active metal sites. Huang et al. (2011) prepared a series of Ni–Mo/SBA-15 bimetallic catalysts, found that Mo species plays an important role in effectively reducing amount of carbon deposition (shell-like) in methane reforming reaction with carbon dioxide, so, keep stability in long test period. The acidity of SiO_2 is too weak to catalyze the cracking reaction. Accordingly, Mo was chosen as the modifier of Ni/SiO_2 catalyst to improve the acidity of support and anti-sintering of Ni in this work. However, the effect of introduction approach of Mo into Ni/SiO_2 upon hydrocarbon cracking activity is ambiguous. Thus, it is necessary to study this effect systematically.

At the same time, Li et al. (2013) investigated that adding high-molecular compound in the process of impregnating the active Ni component can inhibit the contraction of support skeleton as well as the aggregation of metal particle under high temperature, make the Ni species enter into the deeper pores of the support, and then strengthen the mutual effect between Ni and SiO_2 carrier, so that dispersion and high temperature stability of Ni species over Ni/SiO_2 catalyst could be greatly improved. Suárez-Toriello et al. (2015) have reported that citric acid (CA) provided an isolation effect on active metal (Ni) to suppress the aggregation during the pyrolysis on the surface of $Ni/W/Al_2O_3$ catalyst, and CA is freely soluble as well as environment-friendly. Yu e al (Yu et al., 2014). synthesized Ni/CeO_2–Al_2O_3 catalyst by one-step CA method, which decreased the crystallite size and increased the dispersion of Ni species compared with CA-free catalyst, leading to enhanced catalytic partial oxidation activity of methane. In addition, CA molecules can react with the basic and neutral oxhydryl groups on the surface of support to modify the acidity and metal-support interaction of catalyst (Li et al., 2011). Yao et al. (2011) prepared $NiRu/SiO_2$ catalyst in presence of polyethylene glycol (PEG), of which the oligomer group would interact with metal ions (Ni^{2+} or Ru^{3+}) in the aqueous solution so as to form smaller NiO particles (compactly contacting with RuO_2 particles) in contrast to PEG-free process. Meanwhile, Singla et al. (2007) have synthesized the monodisperse Ni nanoparticles in heterogeneous method using cetyltrimethylammonium bromide (CTAB) as stabilizer and Jiang et al. (2013) used CTAB and PEG as organic modifiers to control the size of Ni nanoparticles, which exhibited good catalytic activity. In summary, CA, PEG and CTAB were employed as additives for enhancing the Ni dispersion and inhibiting Ni aggregation in preparation of Ni-based catalysts in published works. Even so, how these organic surfactant additives influence the properties of Ni–Mo/SiO_2 catalysts and application effect in cracking of hydrocarbon (MCH) was investigated in few researches.

Therefore, herein, Ni–Mo/SiO_2 catalysts are synthesized via different loading methods (sol-gel method, co-impregnation and single-impregnation). And their catalytic performances were evaluated by hydrocarbon cracking under supercritical condition so as to screen out the most befitting approach to add active components. Afterwards, the effect of different organic surfactant additives on Ni dispersion as well as catalytic performance was systematically investigated. Meantime, structure-activity relationship of Ni-based catalyst was studied. This contribution will come up with some valuable information for designing high-dispersion Ni-based catalysts and the selection of additives for hydrocarbon fuel cracking.

2. Experimental section

2.1. Catalysts preparation

Sol-gel method was employed to prepare Ni–Mo/SiO_2 catalyst. In typical process, a certain amount of $(NH_4)_6Mo_7O_{24}\cdot 4H_2O$ and $Ni(NO_3)_2\cdot 6H_2O$ were added into acid ludox with stir constantly. Then, water bath at 70 °C for 12 h, grinded into powder on a ball grinder and roasted at 800 °C for 4 h, final catalyst was labeled as NM/S-1. Mo/SiO_2 and SiO_2 supports were also prepared via the similar method. NM/S-2 catalyst using $(NH_4)_6Mo_7O_{24}\cdot 4H_2O$ and $Ni(NO_3)_2\cdot 6H_2O$ as the active components precursor was synthesized through incipient wetness co-impregnation. Meanwhile, NM/S-3 catalyst was synthesized by single-impregnation $Ni(NO_3)_2\cdot 6H_2O$ onto Mo/SiO_2. As-impregnated materials were dried at 50 °C, 70 °C and 95 °C for 1 h, respectively. After dried at 120 °C all night, materials were roasted at 800 °C for 4 h.

The samples with different additives are synthesized through sol-gel method. The additives (CA, PEG, CTAB; Ni/additive = 1 mol ratio) and precursors {$Ni(NO_3)_2\cdot 6H_2O$ and $(NH_4)_6Mo_7O_{24}\cdot 4H_2O$} were mixed evenly and catalyst powders were obtained by the same drying and calcination process described above, and were labeled as NM/S-4, NM/S-5, NM/S-6, respectively. For all the catalysts, the nominal content of MoO_3 and NiO was 5 wt%.

After adequate grind with deionized water and adhesive, the as-prepared catalysts powder coated evenly in the inner surface of SS304 stainless tube (o.d. 3 mm × 0.5 mm and 80 cm) via changing the viscosity of slurry as well as pressure of vacuum pump. In addition, the real coating amount for catalyst is kept at 0.3 ± 0.05 g. The prepared tubular reactors were desiccated at 50 °C, 70 °C and 95 °C for 1 h, severally. During this step, the vapor was swept off with an aurilave. In the end, the tubular reactors were put at 120 °C all night as well as roasted at 500 °C for 2 h.

2.2. Catalysts characterization

The textural properties were characterized on a Quadrasorb SI Automated Surface Area Analyzer (Quantachrome Instruments, USA), and the sample was pretreated at 300 °C under vacuum for 3 h, then the N_2 adsorption-desorption curves was measured at −196 °C. X-ray diffraction (XRD) was recorded on diffractometer (PANalytical B.V., Netherlands), which is equipped with Ni filter and graphite monochromator. The catalyst was measured with Cu Kα (λ = 1.5046 Å) under 40 kV and 25 mA, as well as testing range was from 10° to 90° in sweep speed of 0.03° per second. Acidic characteristics for all samples are analyzed via NH_3-TPD on adsorption analyzer (TP-5076, Tianjin Xuanquan Company). About 0.1 g catalyst particles of 20–40 mesh size obtained by crushed and sieved was activated at 450 °C for 45 min in helium gas (20 mL/min). A

mixture gas (2%NH_3/N_2, 20 mL/min) was adsorbed by the sample for 1 h at 80 °C. Then, the temperature of sample is turned to 800 °C in speed of 10 °C per minute in the helium gas. Finally, the outlet NH_3 was monitored with thermal conductivity detector (TCD). The Brønsted and Lewis acid sites of NM/S-1 and NM/S-4 catalysts were determined by in-situ DRIFTS using NH_3 as probe molecule on a Nicolet 6700 FTIR spectrometer (Thermo fisher, USA) with an MCT detector. The X-ray photoelectron spectroscopy (XPS) was executed on spectrometer (Thermo Scientific Escalab 250) with Al Kα (1486.8 eV) radiation. The reducibility of catalysts and interaction between Ni and Mo or support were analyzed by H_2-TPR on the same adsorption analyzer. 0.1 g sample (20–40 mesh) was activated at 450 °C for 45 min in N_2 gas (20 mL/min). The gas flowing was changed into 20 mL/min mixed gas (5%H_2 in N_2) under room temperature, as well as the catalysts were heated to 900 °C in speed of 10 °C per minute. In addition, the consumption of H_2 was detected with a TCD. High resolution transmission electron microscopy (HRTEM) testing was performed on a Talos-SG (FEI, USA) microscope and the NiO particle size distribution was obtained by Image J software from HRTEM images with at least 150 particles. Meantime, Si, O, Mo and Ni were detected by High-angle annular dark-field (HAADF) and an energy dispersive spectrometer (EDS) mapping.

2.3. Catalytic activity evaluation and products analysis

Cracking performance evaluation of catalysts using MCH as probe compound was operated on self-made equipment, presented in Fig. 1, including fuel feeding section, tubular reactor, condensation separation section as well as product analysis section. Prior to each evaluation, high-purity N_2 was introduced into the whole equipment channel to remove residual gases.

1-fuel tank, 2-high-pressure constant flow pump, 3-Coriolis mass flowmeter, 4-pressure transducer, 5-data acquisition system (HIOKI, Japan), 6-tubular reactor, 7-power regulator, 8-temperature monitor, 9-condenser, 10-filter, 11-back pressure valve, 12-gas-liquid separator and 13, 14- PerkinElmer GC Clarus 680.

For guaranteeing the accuracy of experimental data, parallel tests were performed on each catalyst with the relative error less than 2%. Firstly, MCH (1.0 g/s) was introduced into reaction tube via high-pressure constant flow pump (P270, Dalian Elite Analytical Instruments Co., Ltd.). Coriolis mass flowmeter (CMF010M323, Emerson, uncertainty of ±0.1%) was employed to monitor mass flow rate. And reaction temperature in reaction tube was controlled in the range of 550–750 °C (supervised by sheathed thermocouple with uncertainty of ±2 °C) with the interval of 50 °C (maintain more than 6 min at each target temperatures) through regulating heating power. At the same time, system pressure was maintained at 4.0 ± 0.05 MPa (uncertainty: ±0.5%) with backpressure valve. Subsequently, the high temperature fluid was condensed quickly through water-condenser to eliminate secondary reaction. Gas product was separated from liquid product in gas-liquid separator and raffinate was collected. Gaseous products analysis was completed on PerkinElmer GC Clarus 680 installed with HP-Al/S capillary column (50 m × 0.53 mm, Agilent Technologies Co., Ltd.) as well as flame ionization detector (FID). H_2 was analyzed in a 2 m packed column (stationary phase, TDX-01) as well as TCD in the external standard method. Meanwhile, liquid products are identified on another PerkinElmer GC Clarus 680, equipped with a FID and Elite-Petro column (100 m × 0.25 mm) under certain test conditions (column temperature: 35 °C for 10 min, 50 °C for 55 min, as well as 200 °C for 118 min).

For this contribution, MCH gas yield (Y_G) and conversion (X_C) were calculated according to following equations:

$$Y_G = \frac{M_i - M_l}{M_i} \times 100\% \quad (1)$$

$$X_C = \frac{M_i - M_o}{M_i} \times 100\% \quad (2)$$

where M_i represents inlet mass of fuel, g; M_l represents mass of liquid products, g; and M_o represents mass of fuel in residual, g.

Heat sink (H_s, MJ/kg) was calculated by equation (3):

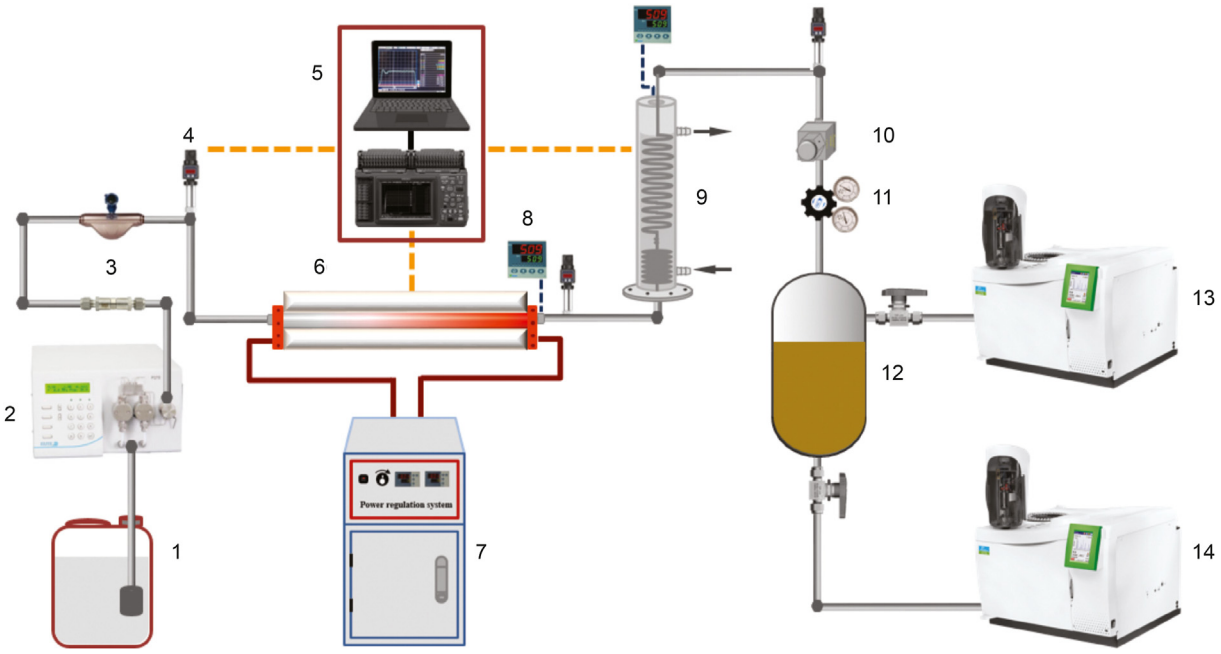

Fig. 1. Schematic sketch for performance evaluation equipment.

$$H_s = \frac{U \cdot I \cdot \eta}{1000 \times f} \quad (3)$$

where U is heating voltage, V; I is heating current, A; f represents mass flow rate, g/s; as well as η represents power conversion rate, which is controlled at about 97% by strengthening heat insulation.

After the whole cracking process, the coke for last 5 cm tubular reactor was detected on CO_2 infrared analyzer at 900 °C and amount was calculated in formula below.

$$m = \frac{M}{S} = \frac{M}{2 \times 5 \cdot \pi \cdot r_i} \quad (4)$$

where m is the average amount of coke for last 5 cm tubular reactor, mg/cm^2; M is the total quantity of coke in reactor, mg; S represents superficial area of reactor, cm^2 as well as r_i represents the inner radius of tubular reactor, cm.

3. Results and discussion

3.1. Effect of preparation method on the structure and activity of Ni–Mo/SiO2 catalyst

3.1.1. Catalytic performance

3.1.1.1. Products distribution and carbon deposition. In the gaseous products, some desirable products (hydrogen and alkenes) contributed to the enhancement of heat sink and Formation of saturated alkanes is to the disadvantage of increasing the heat sink. Gaseous products distribution of MCH cracking is shown in Fig. 2a–e. And the gas products were primarily composed of hydrogen (H_2), small molecule alkanes (methane, ethane, propane and butane) and alkenes (ethylene, propylene, butene and 1,3-butadiene). Apparently, the content of H_2 decreases while the alkenes, especially ethylene, increase with temperature. At relative low temperature, content of H_2 produced during catalytic cracking is higher, but with the further increase of temperature, the H_2 content is gradually lower in contrast to thermal cracking (TC). The C–H bond is easier to break than C–C bond as well as the degree of cracking reaction is poor at low temperature (Jiao et al., 2013). Thus, the content of H_2 in the product is higher, which also shows that the selectivity to H_2 of catalytic cracking is better at low temperature. However, the C–C bond becomes easily broken with the increase of temperature, and the content of other products increases, so the relative content of H_2 decreases. Have to say, methane is primary products (ca. 30%) in the gaseous products, this is because the methyl group on the ring is easy to come off. The contents of alkanes (methane, ethane, propane and butane) just fluctuate up and down with the temperature slightly. Unfortunately, there is no obvious difference between gas products of the hydrocarbon cracking over the catalysts and thermal cracking. In other word, these catalysts rarely increased the selectivity of desirable products compared with TC.

The composition of liquid-phase products is too complex to list detailedly so that this work mainly summarizes several kinds of substances (paraffins, olefins, cycloalkanes, aromatics) with high content, as presented in Table S1 in the Supporting Material. Furthermore, compared with TC, catalytic cracking produced more olefins and aromatics in liquid products. Aromatics content increases with temperature, while olefin fraction climbs up and then decline. To our best knowledge, process of the hydrocarbon catalytic cracking is carried out based on the mechanism of carbenium

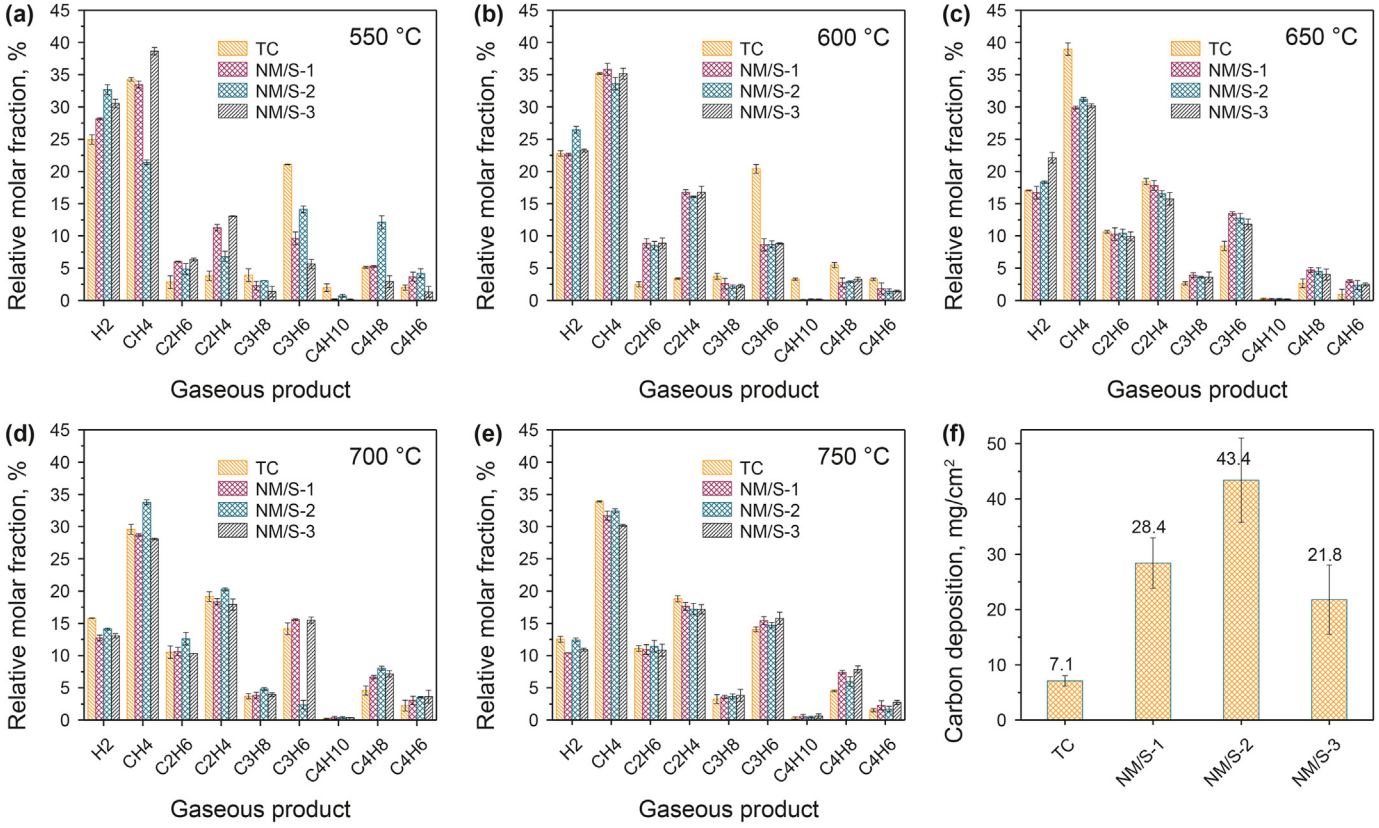

Fig. 2. Gaseous products distribution at different temperature and amount of carbon deposition (f) of MCH cracking over NM/S-1, NM/S-2 and NM/S-3. (a) 550 °C, (b) 600 °C, (c) 650 °C, (d) 700 °C and (e) 750 °C.

ion. Carbenium ion is unstable and then continues to conduct β-scission or isomerization reaction, resulting extensive olefins. However, with the increasing of temperature, olefins undergo secondary reactions such as dehydrogenation, cyclization, polymerization, etc., producing more aromatic hydrocarbons or even carbon deposition (Cumming and Wojciechowski, 1996). This also explains the decrease of olefins content and the increase of aromatics content in the corresponding liquid products of the catalyst. Obviously, aromatics (precursor of coking) of MCH cracking products over NM/S-1 is the highest relative ratio under high temperature (≥600 °C) among these catalysts, indicating that NM/S-1 used for MCH cracking possessed deeper cracking depth and higher coking trend.

As depicted in Fig. 2f, the average amount of coke during catalytic cracking increased in comparison to that of TC (7.1 mg/cm^2), which is related to the deeper cracking degree and higher amount of carbon deposition precursor (aromatics) in the above-mentioned products distribution. The average amount of coke sequence was NM/S-2 (43.4 mg/cm^2) > NM/S-1 (28.4 mg/cm^2) > NM/S-3 (21.8 mg/cm^2).

3.1.1.2. Gas yield, conversion and heat sink. Gas yield as well as conversion for hydrocarbon cracking were employed to assess catalytic cracking activity of catalysts. Furthermore, their variation with temperature is demonstrated in Fig. 3. With the increment of cracking temperature, the gas yield increased, especially the catalytic cracking. It shows that the temperature has an effect on the cracking depth, and the NM/S-1 catalyst has an obvious promoting effect on cracking with more small molecular products (gaseous products) than TC.

Physical heat sink of methyl cyclohexane is obtained using SUPERTRAPP program of NIST and the variation of heat sink is presented in Fig. 4. As we all know, hydrocarbon fuel cracking reaction was endothermic. Therefore, high MCH conversion and yields of small hydrocarbon products are helpful to release more chemical heat sink (Kim et al., 2012). It shows that the gas yield, conversion as well as heat sink increased with temperature. Under the identical experimental conditions, the cracking degree and heat sink of MCH increased in sequence of TC ≈ NM/S-3 < NM/S-2 < NM/S-1. The gas yield and conversion between 650 °C and 700 °C increase more compared to the increase of the heat sink between 650 °C and 700 °C. Actually, this is because that the physical heat sink is the main of heat sink and the variations of gas yield and conversion for EHF is close to chemical heat sink, as shown in Fig. S2. At 750 °C, the MCH conversion and heat sink over

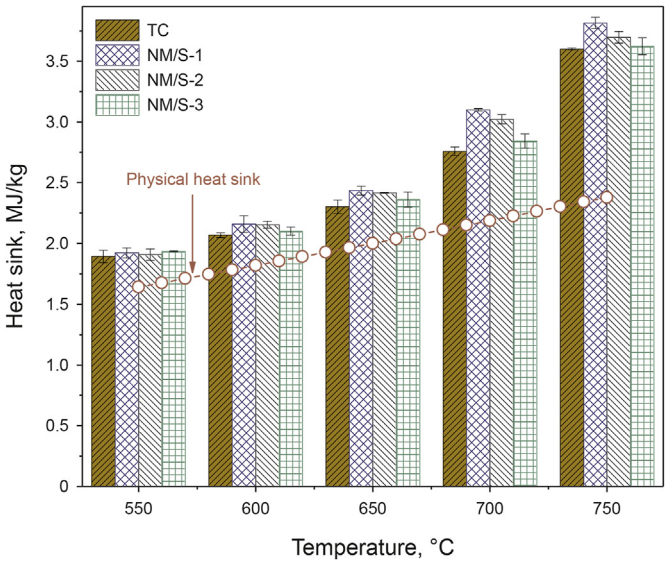

Fig. 4. Heat sink of MCH cracking over NM/S-1, NM/S-2 and NM/S-3.

NM/S-1 catalyst increased by 22.9% and 0.21 MJ/kg in contrast to those of TC, respectively. Meanwhile, chemical heat sink of MCH over NM/S-1 increased by 17.6% compared with TC. Heat sink was obtained an optimum (3.81 MJ/kg) over NM/S-1 catalyst at 750 °C, which has the best MCH conversion (81.1%) and gas yield (50.6%).

3.1.2. Structure-activity relationship of catalyst

The N_2 adsorption-desorption isothermals of Ni–Mo/SiO_2 catalyst obtained by diverse synthesis method are displayed as Fig. 5a. Obviously, isothermals of the catalysts presented representative form IV hysteresis loop. This proves these samples are mesoporous (2–50 nm) materials. Meantime, specific surface area (S_g m^2/g), pore volume (V_P, cm^3/g) and average pore diameter (D_{pore}, nm) are summarized in Table 1. NM/S-2 catalyst owns the largest S_g (116.9 m^2/g) and V_P (0.44 cm^3/g), followed by NM/S-1 (87.1 m^2/g, 0.39 cm^3/g) and NM/S-3 catalyst (55.9 m^2/g, 0.26 cm^3/g). The higher S_g is to the benefit of the dispersion, as well as the larger pore volume can reduce the mass transfer resistance, which is conducive to the cracking reaction. However, the textural properties are not the main factor of influencing the cracking activity (Zhang et al., 2020). Fig. 5b shows the XRD patterns of NM/S-1, NM/S-2 and NM/S-3 catalysts. The diffraction peaks appeared at 2θ of

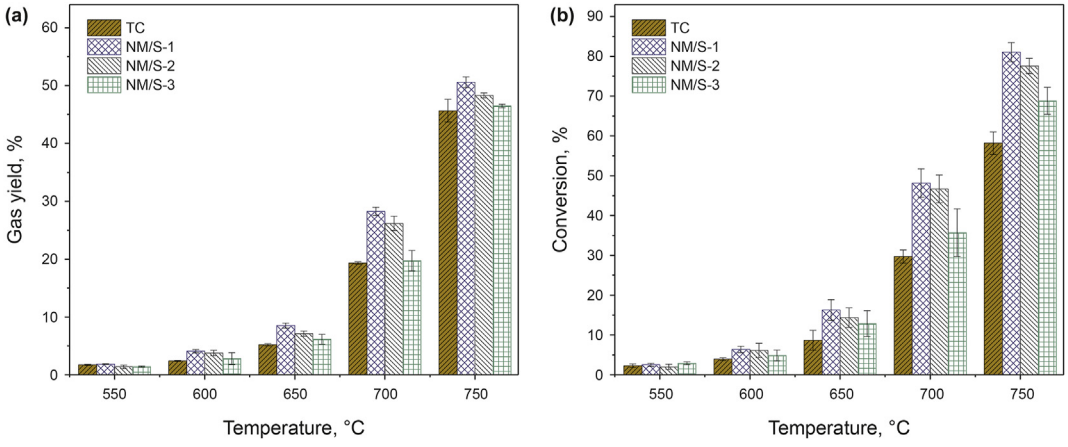

Fig. 3. Gas yield (a) and conversion (b) of MCH cracking over NM/S-1, NM/S-2 and NM/S-3.

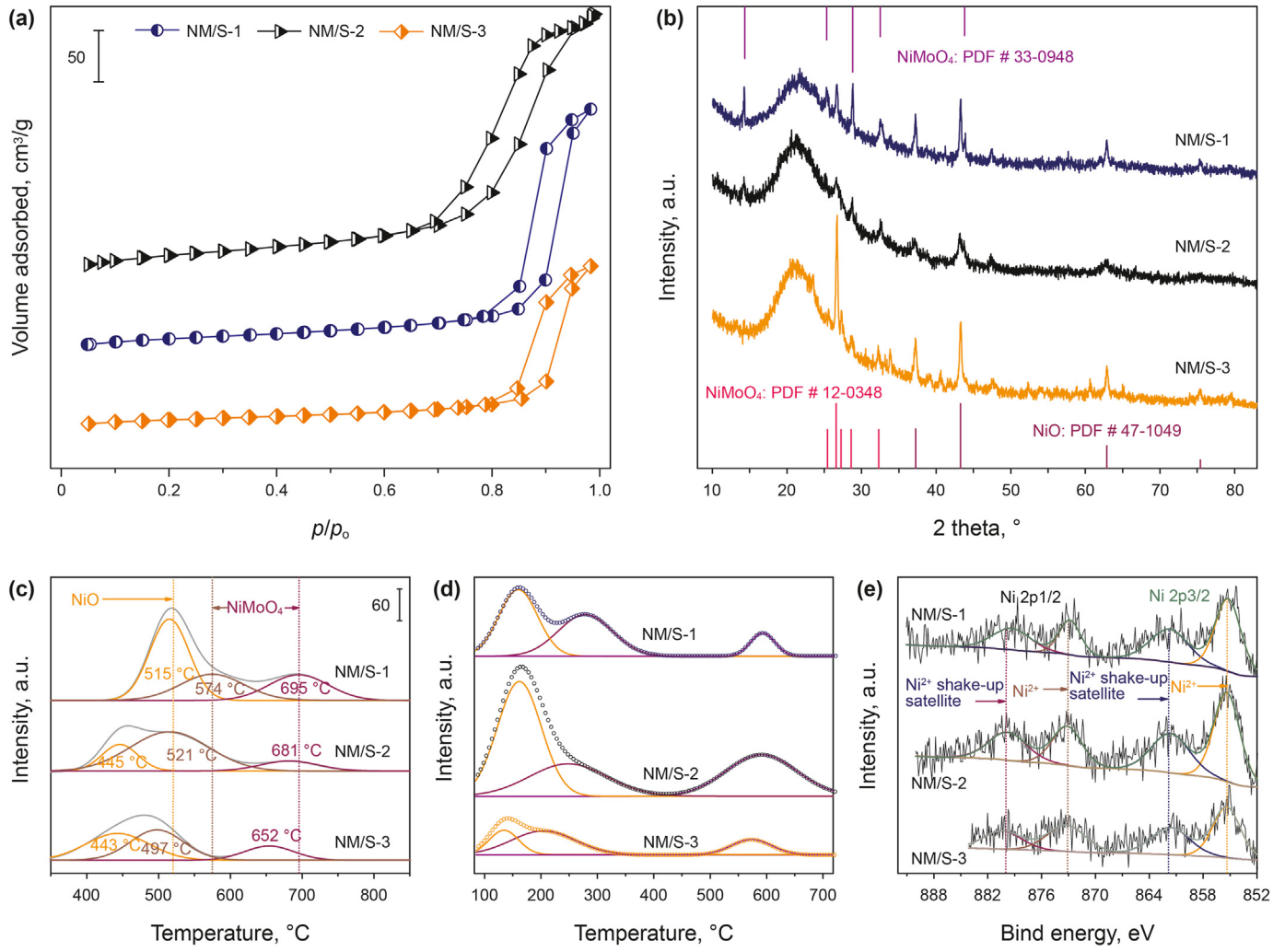

Fig. 5. Characterization results for catalysts by different preparation methods. (a) N_2 adsorption-desorption isotherms, (b) XRD patterns, (c) H_2-TPR patterns, (d) NH_3-TPD profiles and (e) XPS spectrums.

Table 1
Textural properties and acid sites distribution of NM/S-1, NM/S-2 and NM/S-3.

Samples	Texture properties			Peak temperature, °C			Acid sites, μmolNH_3/g		
	S_g, m^2/g	V_P, cm^3/g	D_{pore}, nm	Weak	Medium	Strong	Weak	Medium	Strong
NM/S-1	87.1	0.39	8.8	160.9	278.6	593.2	8.4	7.3	1.8
NM/S-2	116.9	0.44	4.8	160.8	248.3	591.0	15.3	7.6	9.0
NM/S-3	55.9	0.26	8.7	134.5	204.2	573.3	2.1	4.5	1.8

37.2, 62.9 and 75.4° for all samples are attributed to NiO phase (JCPDS card number: 47–1049). SiO_2 phase was detected according to JCPDS card number:39–1425. And all remaining diffraction peaks can be assigned to $NiMoO_4$ phase. In addition, no diffraction peaks of other oxides are found, which may be that the oxides do not exist or their grain size is less than the minimum detection limit (<4 nm) of X-ray diffraction. Interaction between active components and support of Ni–Mo/SiO_2 prepared by different methods and reducibility of catalysts were proved by H_2-TPR, as demonstrated in Fig. 5c. It is apparent that the peak temperatures for NM/S-1 corresponding to reduction of dissociative NiO, $NiMoO_4$ and NiO weakly interacting with support, and $NiMoO_4$ strongly interacting with support, were higher than NM/S-2 and NM/S-3 catalysts wholly. This indicates that the Ni–Mo/SiO_2 synthesized by sol-gel method possessed stronger interaction between active components and support compared with co-impregnation and single-

Table 2
H_2 consumption of different catalysts prepared by different methods.

Samples	H_2 consumption, μmol/0.1g_{catal}			
	Low-temperature peak		High-temperature peak	Total
	NiO	$NiMoO_4$	$NiMoO_4$	
NM/S-1	30.3	15.6	14.4	60.3
NM/S-2	10.8	35.4	6.5	52.7
NM/S-3	19.4	18.2	8.0	45.6

impregnation. Furthermore, H_2 consumption of different catalysts was calculated and listed in Table 2 based on H_2-TPR testing. NM/S-1 owns the maximum reducible species (60.3 μmol/0.1g_{catal}) on the surface of catalyst in contrast to NM/S-2 and NM/S-3. NH_3-TPD technology is used for studying the acidity characteristics (amount of acid site and acid strength) of Ni–Mo/SiO_2 catalyst, and the results are presented in Fig. 5d and Table 1. It is apparently that NH_3 adsorbed on catalyst surface gradually desorbed with the increase of temperature and all catalysts have three desorption peaks, which indicated that there were many kinds of acid sites and the acid strength was non-uniform and continuous distribution. The desorption peak at low temperature (100–200 °C) are attributed to weak acid sites, the desorption peak at moderate temperature (200–400 °C) are correspond to medium acid sites, and the desorption peak at high temperature (>400 °C) are assigned to strong acid sites. The results of quantitative analysis of acid sites showed that the total acid amount of NM/S-2 catalyst was the highest, up to 32.0 μmolNH_3/g, while the total acid amount of NM/S-1 and NM/S-3 catalysts decreased to 17.6 μmolNH_3/g and 8.3 μmolNH_3/g, respectively. Furthermore, electronegativity of support can be changed by Mo species, thereby, the acidity of support was altered. XPS fine spectrum of Ni 2p is presented in Fig. 5e. It is obviously that the bind energy of Ni 2p for these three catalysts was similar and the order of peak intensity was same with the sequence of specific surface area, suggesting that Ni species exist on the surface for three catalysts in same valence state (Ni^{2+}) and amount of Ni species on the external surface was closely associated to textural properties.

Many studies (Hou et al., 2017; Lin et al., 2015; Wang et al., 2017) have shown that the breaking rate of C–C bond is strengthened with strong acid sites content. However, carbon deposition shows positive correlation with amount of acid sites during the catalytic cracking. Although NM/S-2 owns the most amount of strong acid sites (9.0 μmolNH_3/g), excess total amount of acid sties results in carbon deposition covering the active sites so that the cracking activity was lower than NM/S-1, which is in accordance with carbon deposition results. Meanwhile, the reducible species on the surface of NM/S-2 catalyst is less, suggesting that there are less active metal sites on the surface of NM/S-2 in contrast with NM/S-1 catalyst. Additionally, these can explain that conversion and heat sink for NM/S-2 are similar to NM/S-1 under low temperature (≤650 °C). In the case of NM/S-3, it owns the same amount of strong acid sites with NM/S-1, specific surface area (55.9 m^2/g) of NM/S-3 is too small to disperse active components on the support uniformly and to provide place for large-molecule MCH cracking, this is the reason why the heat sink over it was close to TC. Thus, NM/S-1 have the best catalytic cracking activity. To sum up, Ni–Mo/SiO_2 with strong interaction between active components and support synthesized by solgel method can obtain more active metal sites as well as appropriate acidity compared with co-impregnation method and kept good textural properties in comparison to single-impregnation. Therefore, the activity difference of catalyst synthesized in different methods is primarily due to the difference in active sites, acidity and texture properties.

3.2. Effect of additives on the structure and activity of Ni–Mo/SiO2 catalyst

3.2.1. Catalytic performance

3.2.1.1. Product distribution and carbon deposition. In this contribution, thermal and catalytic cracking of MCH occur simultaneously in the microchannel under such large mass flow rate (1 g/s) so that the cracking process is too complicated to obtain the specific reaction steps between different catalysts in detail, which lead to the difference of products. In other word, the cracking mechanism is difficultly obtained according to the analysis of pyrolysis products in this work. However, the variation of some products can help to understand the performance of the catalysts. Even if not all the products show a clear pattern of change, gaseous products distribution is presented in Fig. 6a–e and liquid products distribution is listed in Table S2 in the Supporting Material. Apparently, the H_2 value for all the catalysts reduces with temperature and methane is the main gas product (28%–44%). It can be seen that introduction of additive in Ni–Mo/SiO_2 catalyst changed the gaseous product components of MCH cracking rarely. NM/S-4 catalyst under 550 °C and 600 °C exhibited higher H_2 selectivity than others. The explanation for this may be similar with above discussion of gas product that it is prone for NM/S-4 to boost the breakage of C–H under low temperature but fracture of C–C under high temperature (≥650 °C). Meantime, the content of alkenes (C_2H_4, C_3H_6, C_4H_8 and C_4H_6) increase with temperature (from 550 °C to 700 °C) and then stays flat while methane decreases with temperature (from 550 °C to 700 °C) and then increases. Production of alkenes is in favor of improving the heat sink while alkanes, especially CH_4, is to the disadvantage of. This may be one reason for heat sink increasing with temperature.

In liquid products, amount of olefins presented a trend of increasing at first and then decreasing with temperature (inflection point is 650 °C), which is similar to above discussion about olefins. Under higher temperature (650 °C), secondary reaction of olefines intensified to produce more aromatics. Hence, the aromatics increases with temperature evidently. In addition, the aromatics over these catalysts with additive is more than that over NM/S-1, this suggests that amount of carbon deposition over NM/S-1 is less than that over these modified catalysts due to more coking precursor in the liquid products. As expected, the amount of coke for Ni–Mo/SiO_2 catalyst with the addition of additives is higher than that (28.4 mg/cm^2) of NM/S-1 catalyst, as depicted in Fig. 6f. This phenomenon can be on account of higher cracking depth after introduction of additives, which would be discussed later. Meantime, the amount (34.3 mg/cm^2) of carbon deposition over NM/S-4 is the least among these catalysts with additive.

3.2.1.2. Gas yield, conversion, heat sink and stability. Fig. 7 shows the gas yield as well as conversion data for methyl cyclohexane catalytic cracking in the range of 550–750 °C. Gas yield and conversion, which can reflect the cracking depth of MCH, for catalysts are in the order of NM/S-4 > NM/S-5 > NM/S-6 > NM/S-1. This order can demonstrate the reason for results of coke above and that introduction of additive in Ni–Mo/SiO_2 can promote the production of small molecular gas products. It is interesting noting that the cracking conversion over the NM/S-4 is the highest among catalysts with additives, but the amount of carbon deposition is the least, implying that NM/S-4 can resist carbon deposition to some degree. Meanwhile, the higher conversion (gas yield) and better selectivity for H_2 and unsaturated hydrocarbons of catalytic cracking reaction also contribute to improve heat sink.

As shown in Fig. 8, NM/S-4 has the best heat sink at each target temperature, especially at 750 °C, NM/S-4 catalyst has the best heat sink (3.99 MJ/kg), which is positively related to its highest conversion (89.9%) and the better olefins selectivity. Nevertheless, the carbon deposition is the hardest issue for catalytic cracking over the Ni-based catalyst and gradually cover the active sites with the as the reaction progress. In consequence, the cracking stability of NM/S-4 catalyst was evaluated under 750 °C and 3.5 MPa within 30 min on stream and evaluation was repeated three times. In this process, the heat sink and gas yield of MCH cracking were regarded for index to estimate the stand or fall. It is observed that the activity of NM/S-4 at 15th minute (3.865 MJ/kg) declined a little bit in comparison to that at 5th and 10th minutes because of carbon

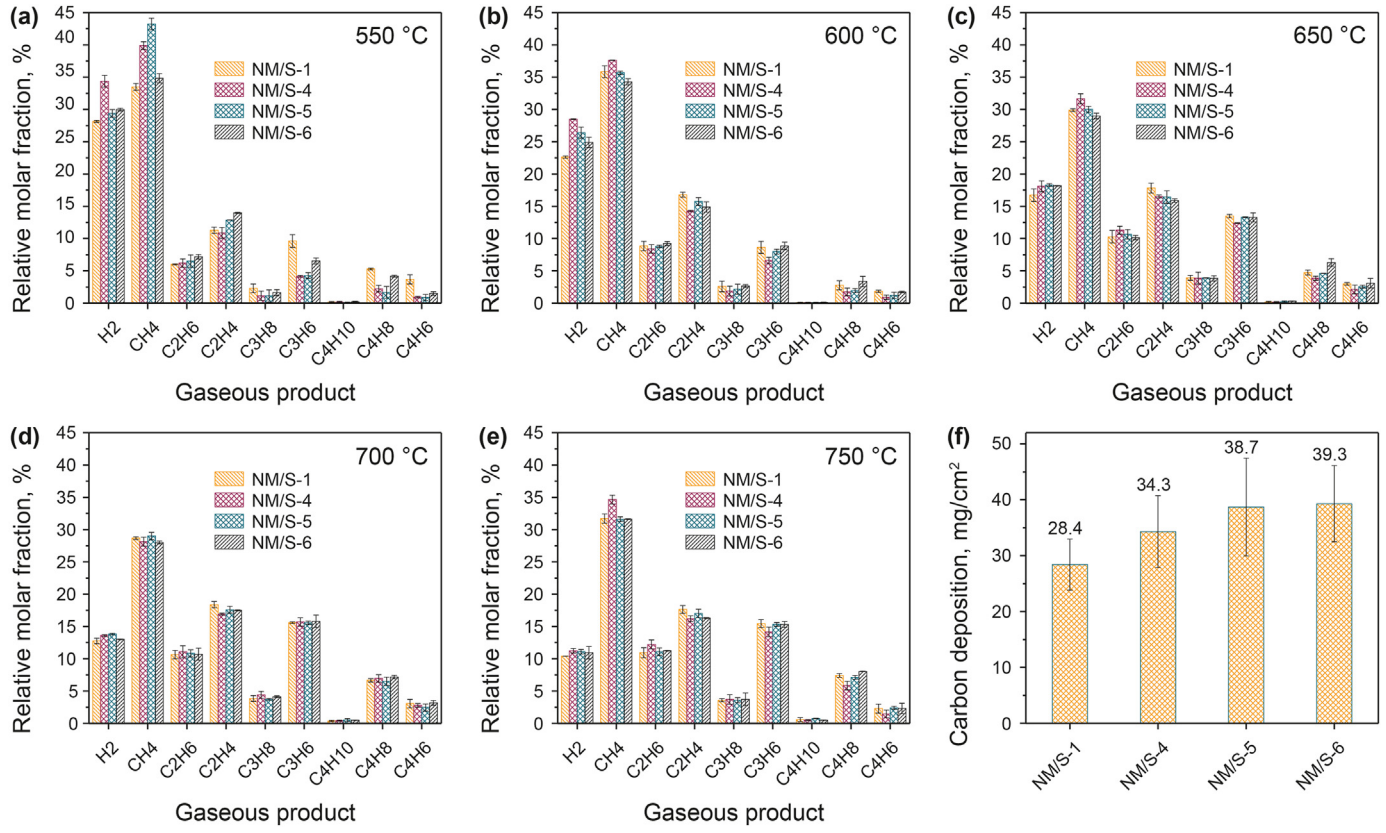

Fig. 6. Gaseous products distribution at different temperature and amount of carbon deposition (f) of MCH cracking over catalysts with addition of additives. (a) 550 °C, (b) 600 °C, (c) 650 °C, (d) 700 °C and (e) 750 °C.

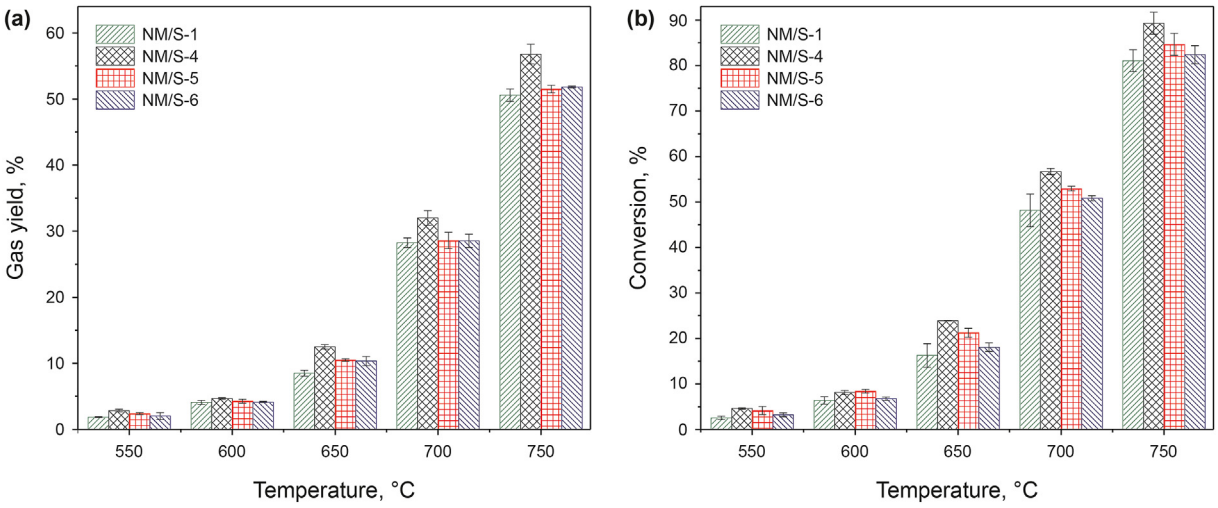

Fig. 7. Gas yield (a) and conversion (b) of MCH cracking over catalysts with addition of additives.

depositing on the surface of catalyst coating gradually. Unfortunately, the heat sink and gas yield at 20th minute descended to 3.695 MJ/kg and 51.8%, severally. Between the 15th and 20th minute, the carbon deposition nearly covered the catalyst coating that coke inhibited the contact between reactant molecule and active sites of catalyst. After that, the reaction performances, being heat sink of 3.647 MJ/kg and gas yield of 46.5%, were close to thermal cracking.

3.2.2. Structure-activity relationship of catalyst

As shown in Fig. 9a and Table 3, the adsorption-desorption isotherm characteristics of all catalysts were similar, and the hysteresis ring appeared after $p/p_0 > 0.8$ in all catalysts. The textural properties of NM/S-1, NM/S-4 and NM/S-6 catalysts were not significantly different, indicating that the introduction of CA and CTAB has little impact on the texture properties of Ni–Mo/SiO_2 catalysts. For NM/S-5 catalyst, PEG plays a role of pore expanding agent in the process of preparation (Li et al., 2008), and PEG with

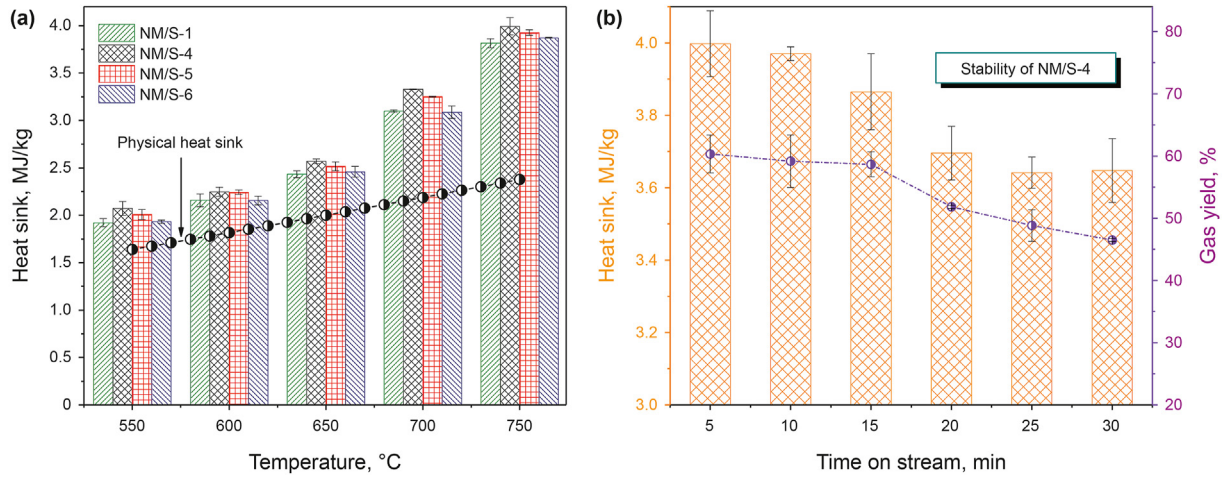

Fig. 8. (a) Heat sink of MCH cracking over catalysts with addition of additives and (b) stability of NM/S-4 catalyst (Experimental conditions: pressure, temperature and mass flow rate are kept at 4.0 MPa, 750 °C and 1 g/s, respectively).

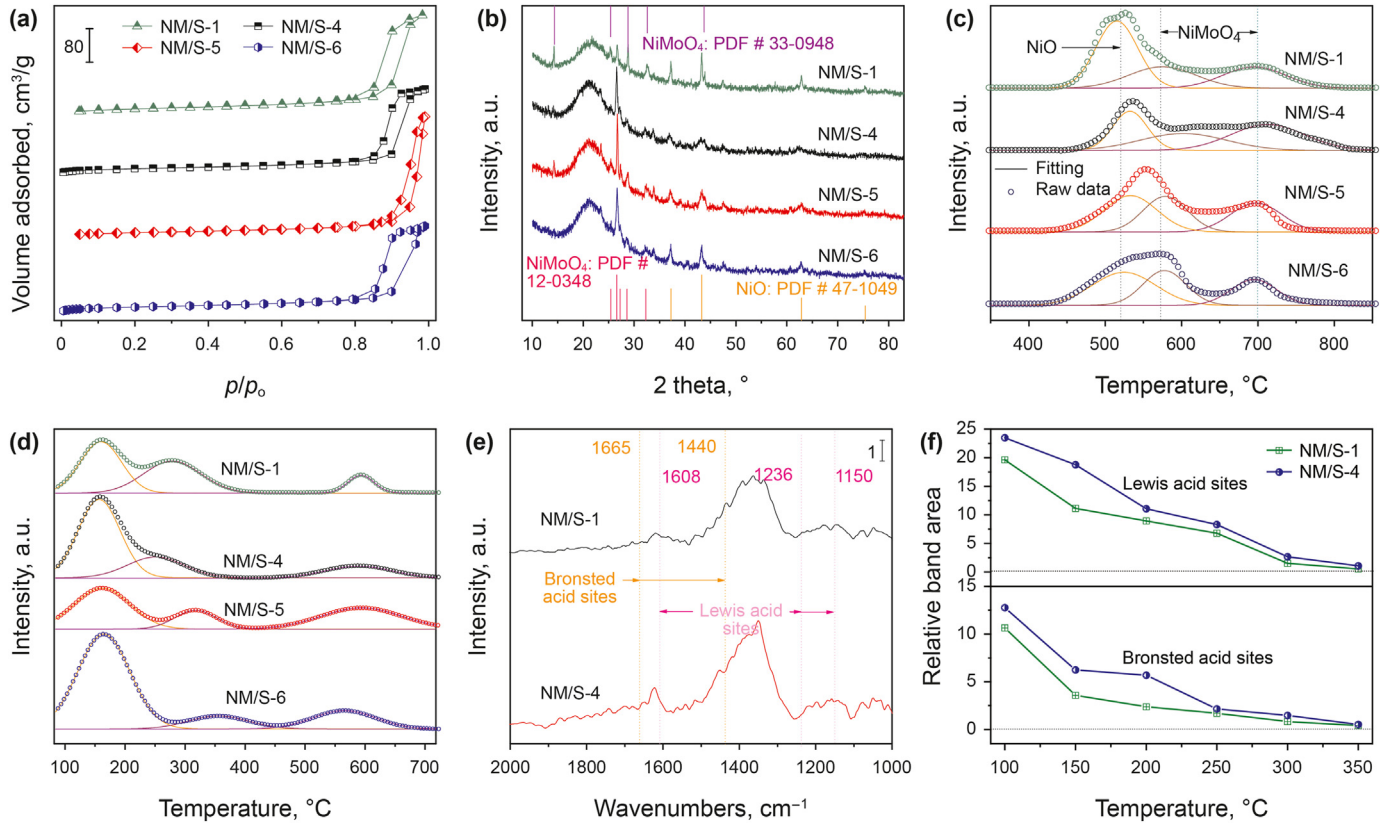

Fig. 9. Characterization results for catalysts with addition of different additives. (a) N_2 adsorption-desorption isotherms, (b) XRD patterns, (c) H_2-TPR profiles, (d) NH_3-TPD patterns, (e) IR spectra with NH_3 desorption at 100 °C of NM/S-1 and NM/S-4 as well as (f) the contributions of the Lewis and Brønsted acid sites over the of NM/S-1 and NM/S-4.

Table 3
Textural properties as well as acid sites distribution for different catalysts with addition of additives.

Samples	Texture properties			D_{Ni}, nm	Acid sites, μmolNH_3/g				
	S_g, m^2/g	V_P, cm^3/g	D_{pore}, nm		Weak	Medium	Strong	Total	Density, μmolNH_3/m^2
NM/S-1	87.1	0.39	10.7	24.7	8.4	7.3	1.8	17.6	0.20
NM/S-4	70.3	0.34	9.5	11.9	12.2	4.4	3.0	19.6	0.28
NM/S-5	50.2	0.45	17.3	13.6	9.3	3.2	6.9	19.4	0.39
NM/S-6	77.3	0.35	7.9	17.4	19.9	3.1	4.6	27.6	0.36

strong hydrophilicity competes with silica gel particles for the hydration layers (Jiang et al., 2012), which makes silica gel particles grow easily, resulting in the largest pore volume (0.45 cm^3/g), mean pore radius (17.3 nm) and smaller specific surface area (50.2 m^2/g).

The XRD patterns of catalysts with additives added in the preparation process are shown in Fig. 9b. As we can see, there are two types of diffraction peaks of NiO phase (JCPDS card number: 47–1049) and $NiMoO_4$ phase in all samples. However, after adding additives, the JCPDS card number of $NiMoO_4$ phase changed from 33 to 0948 to 12–0348, and the intensity of NiO diffraction peak was weakened. Meanwhile, NiO crystallites size (D_{Ni}) of all catalysts calculated through Scherrer formula in line with Ni (111) crystal face diffraction peaks were listed in Table 3. And the order of NiO grain size is: NM/S-4 (11.9 nm) < NM/S-5 (13.6 nm) < NM/S-6 (17.1 nm) < NM/S-1 (24.7 nm), demonstrating the addition of additives can inhibit the agglomeration of NiO to obtained smaller crystallite size, this is to say that the catalysts have good dispersibility of active components (Ni). In order to further comprehend the Ni dispersion on the catalyst, the NM/S-4 catalyst with optimal cracking activity was investigated by HRTEM, HAADF-STEM and elemental mapping. Intuitively, it can be seen from Fig. 10a (TEM picture) that the Ni particles dispersed on the surface of SiO_2 support uniformly with introducing the CA additive. At the same time, the lattice fringe spacing of 0.20 nm in Fig. 10a1 for NM/S-4 catalyst was indexed to Ni (111) crystal face. As shown in Fig. 10b, Ni particles size measured from TEM picture presented wide distribution ($d = 8.25 \pm 4.12$ nm). In Fig. 10c, red and yellow represented the Ni and Mo elements, severally, which were evenly dispersed on the catalyst, indicating introduction of CA additive suppress the aggregation of active metal.

Fig. 9c demonstrates the H_2-TPR curves for different samples. The reduction of species on the surface of Ni–Mo/SiO_2 catalysts showed two wide peaks at about 550 °C and about 700 °C, respectively. Sridhar et al. (2020) studied the H_2-TPR of Ni–Mo/ZSM-5, and obtained similar reduction peaks at 535 °C and 710 °C, respectively. NiO species isolated on the surface can be reduced under lower temperature (<550 °C) (Zhang et al., 2018). Therefore, the widened and asymmetric low-temperature peaks (450–650 °C) in Ni–Mo/SiO_2 catalysts were attributable to the superposition peaks of reduction peaks of $NiMoO_4$ spinel and NiO species interacting with support weakly. And the reduction peak near 700 °C was on account of production of stable $NiMoO_4$ spinel interacting with support strongly. In addition, the quantitative results of the TPR profiles were summarized as Table 4. It is worth noting that the total H_2 consumption (about 60 μmol/0.1g catalyst) of all catalysts remains basically consistent. However, compared with NM/S-1

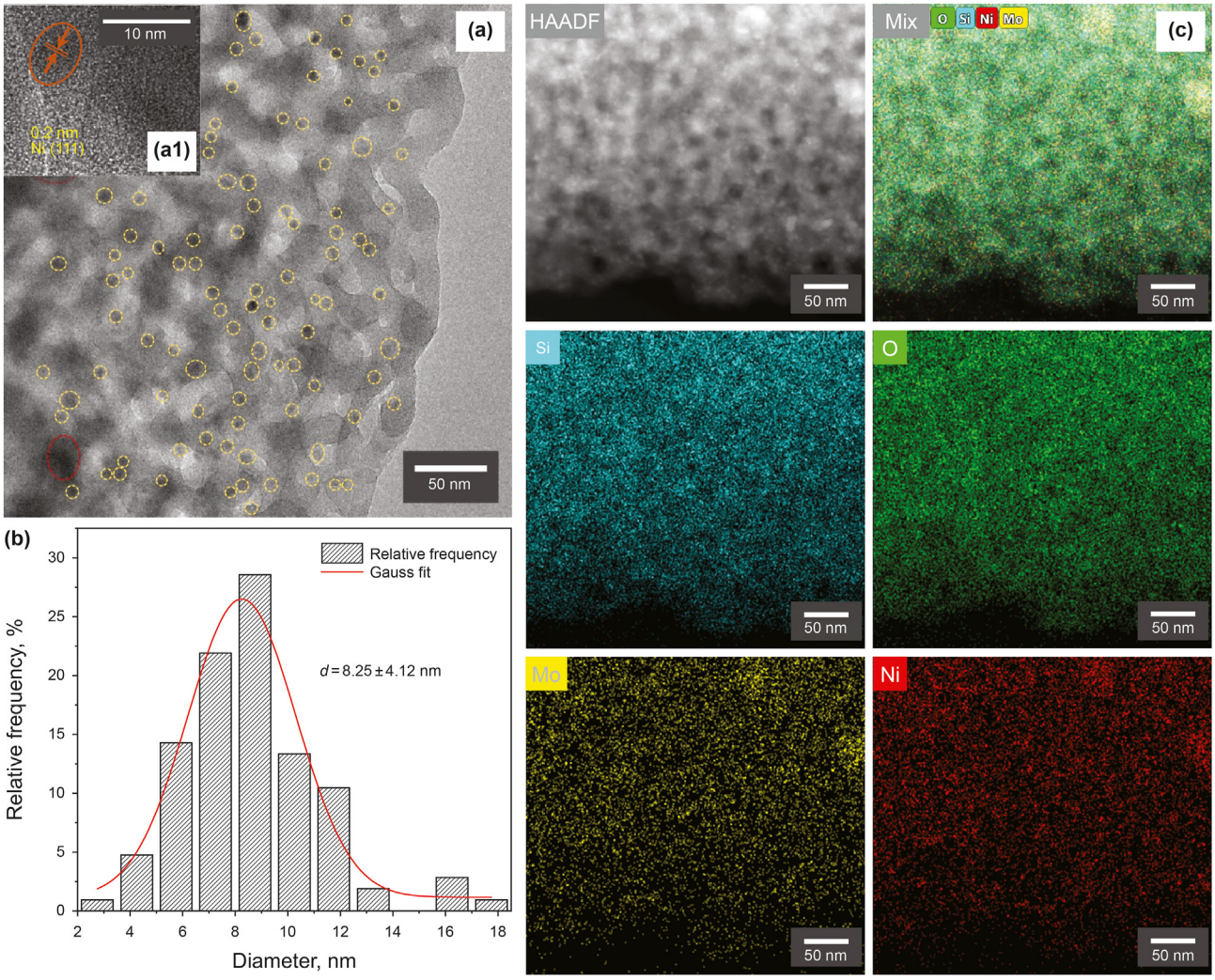

Fig. 10. HRTEM and EDS-mapping results for NM/S-4 catalyst. (a) and (a1) HRTEM pictures in different magnification times, (b) particles size distribution of Ni and (c) HAADF-STEM image and Si, O, Mo as well Ni elements distribution (mapping).

Table 4
H_2 consumption of different catalysts with addition of additives.

Samples	H_2 consumption, μmol/0.1g catalyst			
	Low-temperature peak		High-temperature peak	Total
	NiO	$NiMoO_4$	$NiMoO_4$	
NM/S-1	30.3	15.6	14.4	60.3
NM/S-4	16.9	18.4	24.0	59.3
NM/S-5	23.2	19.1	18.1	60.4
NM/S-6	26.3	18.5	14.8	59.6

catalyst, other catalysts have smaller low-temperature reduction peaks as well as larger high-temperature reduction peak, and the H_2 consumptions of high-temperature reduction peak of the three catalysts (NM/S-4, NM/S-5, NM/S-6) are 9.6, 3.7 and 0.4 μmol/0.1g catalyst higher than that of NM/S-1 catalyst, respectively, demonstrating that the additives promoted the strong mutual effect between Ni and Mo, reduces the number of isolated NiO, as well as inhibits the agglomeration of NiO species to a certain extent, which agrees with the XRD characterization results.

Obviously, the acidity of catalyst has an important influence on the activity of cracking reaction. Fig. 9d presents the NH_3-TPD curve of catalysts with additives. It is clear that the areas of desorption peaks are completely diverse, suggesting that there are distinct amounts of acid sites for catalysts. We can see from Table 3, compared with NM/S-1 catalyst, the first and third NH_3 desorption peak areas of the catalysts (NM/S-4, NM/S-5, NM/S-6) were larger, while the second desorption peak areas were smaller. In addition, the total acid amount was listed in descending order of NM/S-6 (27.6 μmolNH_3/g) > NM/S-4 (19.6 μmolNH_3/g) > NM/S-5 (19.4 μmolNH_3/g) > NM/S-1 (17.6 μmolNH_3/g), proving that the addition of additives promoted the quantity of weak and strong acid sites on the surface. For further comprehending the role of acid type play in catalytic cracking, the NM/S-1 and NM/S-4 catalysts with significant difference in activity were determined by *in-situ* DRIFTS using NH_3 as probe molecule. The IR spectra for NH_3 species desorption at 100 °C on the NM/S-1 and NM/S-4 catalyst was exhibited in Fig. 9e. The peaks centered at around 1150 cm^{-1}, 1236 cm^{-1} and 1608 cm^{-1} were attributed to N—H bonds in NH_3 linked to Lewis (L) acid sites while the peaks located at 1440 cm^{-1} and 1665 cm^{-1} were ascribed to NH_4^+ absorbed on the Brønsted (B) acid sites (Chen et al., 2018; Xu et al., 2017; Peng et al., 2013). In order to investigated the difference of L and B acid sites between NM/S-1 and NM/S-4, according to references (Chen et al., 2018), the relative band area of adsorbed NH_3 species on L and B acid sites over these two catalysts was calculated via corresponding NH_3 desorption spectra (Fig. S1 in Supplementary Material) with varied temperature, as shown in Fig. 9f. With the temperature increasing, the intensities of these peaks decreased gradually and it hard to be detected at 350 °C. The amount of L acid sites was larger than corresponding B acid sites at each desorption temperature for NM/S-1 and NM/S-4. It is obvious that the amount of L or B acid sites over the NM/S-4 is more than the NM/S-1 catalyst, this is in consistence with NH_3-TPD results. Qu et al. (2011) have reported that L acid sites is the main reason for promoting hydrocarbon cracking and B acid sites are prone to catalyze the carbon deposition. Meantime, B acid sites play a significant role in initiating the reaction to produce carbonium ions for hydrocarbon cracking on the solid acid catalysts (Li et al., 2017). More L and B acid sites on the surface of NM/S-4 is the factor for promoting cracking acitivity and more carbon deposition in contrast to NM/S-1.

Although NM/S-5 catalyst has the largest acid density (0.39 μmolNH_3/m^2) and strong acid sites (6.9 μmolNH_3/g), its average carbon deposition (38.7 mg/cm^2) is lower than NM/S-6 catalyst (39.3 mg/cm^2), which should be closely related to its maximum V_p and mean pore radius, promoting mass transfer rate and strengthening product diffusion (Borm et al., 2010). And the increase of strong acid was beneficial to the catalytic cracking reaction, which increased the conversion as well as heat sink of the reaction. However, the strong acid sites are in the sequence of NM/S-5 > NM/S-6 > NM/S-4 > NM/S-1, which was different from the activity order (NM/S-4 > NM/S-5 > NM/S-6 > NM/S-1). This may be that the addition of additives decreased the particles size of NiO, promoted the high dispersion of the active component NiO and inhibited the aggregation to a certain extent, strengthening the MCH cracking depth. With regard to NM/S-4, deprotonation of carboxylic groups of CA is prone to product (Ni^{2+} and Mo^{6+}) metal-coordination with groups (Suárez-Toriello et al., 2015), which could protect metal from aggregation and increase the interaction between Ni and Mo. This is consistent with results of XRD and more $NiMoO_4$ in results of H_2-TPR. Meantime, the TGA results (In Fig. S3, Supplementary Material) of NM/S-4 demonstrated that the interaction between CA and metal existed actually. In the case of NM/S-5, oligomer of PEG can form coordination bonds with metal cations (Yao et al., 2011). This also can inhibit the aggregation of NiO particles during calcination. Even so, PEG as pore expanding agent results in transformation of textural properties, going against the dispersion of active components. The CTAB including the $CH_3—N^+$ would induce the NiO to stable crystal so that the characteristic peak of NiO in XRD profile was more pointed than other catalysts with additive. Based on the discussion above, the decrease of dissociative NiO, increase of $NiMoO_4$ and smaller grain size lead to more active Ni species over NM/S-4 and increase of strong (and Lewis) acid sites (in contrast to NM/S-1), which are supposed to be responsible to the highest cracking activity and good stability.

4. Conclusions

In this paper, Ni—Mo/SiO_2 catalysts are synthesized through different loading methods and adding additives in sol-gel method. It is obvious that cracking performance for all catalyst is better compared with TC. On the one hand, the loading method for active components affect the properties of catalysts significantly, especially the amount of acid sites. Experimental results display that the Ni—Mo/SiO_2 catalyst synthesized in sol-gel method has better acidity (17.6 μmolNH_3/g total quantity of acid site and 1.8 μmolNH_3/g strong acid sites) and catalytic cracking performance. Interestingly, the quantity of acid sites of catalyst by co-impregnation method with abundant of carbon deposition production is the most, but its activity is lower than that of sol-gel method. Therefore, increasing acidity appropriately can strengthen the cracking performance as well as heat sink of MCH, but excessive acid sites will also increase the amount of coke, covering active sites, thus weakening cracking activity. On the other side, introduction of additives further modified Ni—Mo/SiO_2 catalyst, which increased the transition from medium acid site to strong acid site and adjusted quantity of acid site properly. Moreover, the additives promoted the mutual effect between Ni and Mo, inhibiting the agglomeration of NiO, thus improving the cracking activity and heat sink of MCH. Thereinto, addition of CA into Ni—Mo/SiO_2 has the best promotion in MCH cracking.

Declarations

There are no conflicts to declare.

Author contributions

Jun Zhang, Ting Chen, Yi Jiao and Jian-Li Wang conceived and designed the study. Jun Zhang, Ting Chen, Mei Cheng and Lin-Lin Wang collected data. Jun Zhang, Yi Jiao, Jian-Li Wang, Yao-Qiang Chen and Xiang-Yuan Li analyzed the data. Jun Zhang, Ting Chen, Yi Jiao and Mei Cheng wrote the paper. All authors read and approved the final manuscript.

Acknowledgements

The research was supported by National Natural Science Foundation of China [grant number 91841301] and Fundamental Research Funds for the Central Universities [grant number YJ201791].

Appendix A. Supplementary data

Supplementary data to this article can be found online at https://doi.org/10.1016/j.petsci.2021.08.009.

References

Behnejad, B., Abdouss, M., Tavasoli, A., 2019. Comparison of performance of Ni-Mo/γ-alumina catalyst in HDS and HDN reactions of main distillate fractions. Petrol. Sci. 16, 645–656. https://doi.org/10.1007/s12182-019-0319-5.

Borm, R.V., Reyniers, M.-F., Martens, J.A., et al., 2010. Catalytic cracking of methylcyclohexane on FAU, MFI, and bimodal porous materials: influence of acid properties and pore topology. Ind. Eng. Chem. Res. 49 (21), 10486–10495. https://doi.org/10.1021/ie100429u.

Chen, L.Q., Yuan, F.L., Li, Z.B., et al., 2018. Synergistic effect between the redox property and acidity on enhancing the low temperature NH_3-SCR activity for NO_x removal over the $Co_{0.2}Ce_xMn_{0.8-x}Ti_{10}$ (x=0-0.40) oxides catalysts. Chem. Eng. J. 354, 393–406. https://doi.org/10.1016/j.cej.2018.07.196.

Chin, S.Y., Chin, Y.H., Amiridis, M.D., 2006. Hydrogen production via the catalytic cracking of ethane over Ni/SiO_2 catalysts. Appl. Catal. 300 (1), 8–13. https://doi.org/10.1016/j.apcata.2005.10.031.

Cumming, K.A., Wojciechowski, B.W., 1996. Hydrogen transfer, coke formation, and catalyst decay and their role in the chain mechanism of catalytic cracking. Catal. Rev. 38 (1), 101–157. https://doi.org/10.1080/01614949608006455.

Edwards, T., 2006. Cracking and deposition behavior of supercritical hydrocarbon aviation fuels. Combust. Sci. Technol. 178 (1–3), 307–334. https://doi.org/10.1080/00102200500294346.

Han, Z., Ma, Z., Wang, C.B., et al., 2020. Effect of modified carrier fluoride on the performance of Ni-Mo/Al_2O_3 catalyst for thioetherification. Petrol. Sci. 17 (3), 849–857. https://doi.org/10.1007/s12182-020-00439-9.

He, Z.F., Jiao, Y., Wang, J.L., et al., 2018. Bi-functional composite oxides M(Na, K)-Ni/La-Al_2O_3 catalysts for steam reforming of *n*-decane. Fuel 212, 193–201. https://doi.org/10.1016/j.fuel.2017.10.043.

Hou, X., Qiu, Y., Zhang, X.W., et al., 2017. Analysis of reaction pathways for *n*-pentane cracking over zeolites to produce light olefins. Chem. Eng. J. 307, 372–381. https://doi.org/10.1016/j.cej.2016.08.047.

Huang, F., Wang, R., Yang, C., et al., 2016. Catalytic performances of Ni/mesoporous SiO_2 catalysts for dry reforming of methane to hydrogen. J Energy Chem 25 (4), 709–719. https://doi.org/10.1016/j.jechem.2016.03.004.

Huang, T., Huang, W., Huang, J., et al., 2011. Methane reforming reaction with carbon dioxide over SBA-15 supported Ni-Mo bimetallic catalysts. Fuel Process. Technol. 92 (10), 1868–1875. https://doi.org/10.1016/j.fuproc.2011.05.002.

Jiang, L., Yuan, X., Wu, J., et al., 2012. Effects of preparation conditions of gel method on pore structure of silica-gel carrier. Chemical Research & Application 24, 204–208.. https://doi.org/10.3969/j.issn.1004-1656.2012.02.008 (in Chinese).

Jiang, Z.F., Xie, J.M., Jiang, D.L., et al., 2013. Modifiers-assisted formation of nickel nanoparticles and their catalytic application to p-nitrophenol reduction. CrystEngComm 15 (3), 560–569. https://doi.org/10.1039/C2CE26398J.

Jiao, Y., Wang, J.L., Zhu, Q., et al., 2014. The performance of Pt/$Zr_xTi_xAl_{1-2x}O_2$ as kerosene cracking catalysts. Chin. J. Catal. 35 (2), 175–184. https://doi.org/10.1016/s1872-2067(12)60732-2.

Jiao, Y., Zhang, H., Li, S.S., et al., 2018. Impact of acidity in ZrO_2-TiO_2-Al_2O_3 composite oxides on the catalytic activity and coking behaviors during n-decane cracking. Fuel 233, 724–731. https://doi.org/10.1016/j.fuel.2018.06.011.

Jiao, Y., Wang, J., Qin, L.X., et al., 2013. Kerosene cracking over supported monolithic Pt catalysts: effects of SrO and BaO promoters. Chin. J. Catal. 34 (6), 1139–1147. https://doi.org/10.1016/s1872-2067(12)60541-5.

Kim, J., Park, S.H., Chun, B.H., et al., 2012. Improvement of the heats of reaction in endothermic reactions of methylcyclohexane with zeolites. Catal. Today 185 (1), 47–53. https://doi.org/10.1016/j.cattod.2011.09.020.

Li, G.H., Hu, L.J., Hill, J.M., 2006. Comparison of reducibility and stability of alumina-supported Ni catalysts prepared by impregnation and co-precipitation. Appl. Catal. 301 (1), 16–24. https://doi.org/10.1016/j.apcata.2005.11.013.

Li, H., Li, M., Chu, Y., et al., 2011. Essential role of citric acid in preparation of efficient NiW/Al_2O_3 HDS catalysts. Appl Catal A-gen. 403, 75–82. https://doi.org/10.1016/j.apcata.2011.06.015.

Li, N., Wang, Q., Wang, P., 2008. Properties and structure of Al_2O_3 with large pore. J. Guilin Univ. Technol. 28 (1), 78–81.. https://doi.org/10.3969/j.issn.1674-9057.2008.01.016 (in Chinese).

Li, Q., Hou, Y.H., Dong, L.Y., et al., 2013. Catalytic behaviors and stability of aerogel silica-supported Ni catalysts for the partial oxidation of methane into synthesis gas. Acta Phys. Chim. Sin. 29 (10), 2245–2254.. https://doi.org/10.3866/pku.Whxb201308201 (in Chinese).

Li, S.S., Guo, C.H., Zhang, H., et al., 2017. High hydrogen selectivity and anti-carbon ability by cracking of RP-3 jet fuel over Pt/ZrO_2-TiO_2-Al_2O_3 catalyst modified by M_xO_y (M = Ba, Sr and Ce) promoters. Int. J. Hydrogen Energy 42, 11252–11261. https://doi.org/10.1016/j.ijhydene.2017.03.075.

Lin, L.F., Zhao, S.F., Zhang, D.W., et al., 2015. Acid strength controlled reaction pathways for the catalytic cracking of 1-pentene to propene over ZSM-5. ACS Catal. 5, 4048–4059. https://doi.org/10.1021/cs501967r.

Liu, F., Xu, S.P., Cao, L., et al., 2007. A comparison of NiMo/Al_2O_3 catalysts prepared by impregnation and coprecipitation methods for hydrodesulfurization of dibenzothiophene. J. Phys. Chem. C 111 (20), 7396–7402. https://doi.org/10.1021/jp068482.

Liu, G.Z., Jia, X.K., Tian, Y.J., et al., 2019. Preparations and remarkable catalytic cracking performances of Pt@FGS/JP-10 nanofluids. Fuel 252, 228–237. https://doi.org/10.1016/j.fuel.2019.04.119.

Long, L., Zhou, W.X., Qiu, Y.F., et al., 2020. Coking and gas products behavior of supercritical *n*-decane over NiO nanoparticle/nanosheets modified HZSM-5. Energy 192. https://doi.org/10.1016/j.energy.2019.116540.

Ma, W.C., Liu, B., Ji, X., et al., 2017. Catalytic co-cracking of distilled bio-oil and ethanol over Ni-ZSM-5/MCM-41 in a fixed-bed. Biomass Bioenergy 102, 31–36. https://doi.org/10.1016/j.biombioe.2017.04.006.

Peng, Y., Li, K.Z., Li, J.H., 2013. Identification of the active sites on CeO_2-WO_3 catalysts for SCR of NO_x with NH_3: an in situ IR and Raman spectroscopy study. Appl. Catal., B 140–141, 483–492. https://doi.org/10.1016/j.apcatb.2013.04.043.

Pevneva, G.S., Voronetskaya, N.G., Sviridenko, N.N., et al., 2019. Effect of WC/Ni-Cr additive on changes in the composition of an atmospheric residue in the course of cracking. Petrol. Sci. 17 (2), 499–508. https://doi.org/10.1007/s12182-019-00402-3.

Qin, B., Zhang, X., Zhang, Z., et al., 2011. Synthesis, characterization and catalytic properties of Y-β zeolite composites. Petrol. Sci. 8 (2), 224–228. https://doi.org/10.1007/s12182-011-0139-8.

Qin, J., Zhang, S.L., Bao, W., et al., 2013. Thermal management method of fuel in advanced aeroengines. Energy 49, 459–468. https://doi.org/10.1016/j.energy.2012.10.050.

Qu, S.D., Liu, G.Z., Meng, F.X., et al., 2011. Catalytic cracking of supercritical *n*-dodecane over wall-coated HZSM-5 with different Si/Al ratios. Energy Fuels 25, 2808–2814. https://doi.org/10.1021/ef2004706.

Sim, H.S., Yetter, R.A., Hong, S., et al., 2020. Functionalized graphene sheet as a dispersible fuel additive for catalytic decomposition of methylcyclohexane. Combust. Flame 217, 212–221. https://doi.org/10.1016/j.combustflame.2020.04.002.

Singla, M.L., Negi, A., Mahajan, V., et al., 2007. Catalytic behavior of nickel nanoparticles stabilized by lower alkylammonium bromide in aqueous medium. Appl. Catal. 323, 51–57. https://doi.org/10.1016/j.apcata.2007.01.047.

Sridhar, A., Rahman, M., Infantes-Molina, A., et al., 2020. Bimetallic Mo-Co/ZSM-5 and Mo-Ni/ZSM-5 catalysts for methane dehydroaromatization: a study of the effect of pretreatment and metal loadings on the catalytic behavior. Appl. Catal. 589. https://doi.org/10.1016/j.apcata.2019.117247.

Suárez-Toriello, V.A., Santolalla-Vargas, C.E., De Los Reyes, J.A., et al., 2015. Influence of the solution pH in impregnation with citric acid and activity of Ni/W/Al_2O_3 catalysts. J. Mol. Catal. 404–405, 36–46. https://doi.org/10.1016/j.molcata.2015.04.005.

Wang, Z.Z., Zhang, H., Li, S.S., et al., 2017. The performance of Rh/SiO_2-Al_2O_3 catalysts in methycyclohexane cracking reaction. J. Anal. Appl. Pyrol. 124, 475–485. https://doi.org/10.1016/j.jaap.2017.02.012.

Xu, H.D., Feng, X., Liu, S., et al., 2017. Promotional effects of Titanium additive on the surface properties, active sites and catalytic activity of W/$CeZrO_x$ monolithic catalyst for the selective catalytic reduction of NOx with NH3. Appl. Surf. Sci. 419, 697–707. https://doi.org/10.1016/j.apsusc.2017.05.055.

Yao, N., Ma, H.F., Shao, Y., et al., 2011. Effect of cation-oligomer interactions on the size and reducibility of nio particles on NiRu/SiO_2 catalysts. J. Mater. Chem. 21 (43), 17403–17412. https://doi.org/10.1039/C1JM13029C.

Ye, D.F., Zhao, L., Bai, S.S., et al., 2019. New strategy for high-performance integrated catalysts for cracking hydrocarbon fuels. ACS Appl. Mater. Interfaces 11 (43), 40078–40090. https://doi.org/10.1021/acsami.9b14285.

Yu, C.L., Hu, J.B., Zhou, W.Q., et al., 2014. Novel Ni/CeO_2-Al_2O_3 composite catalysts synthesized by one-step citric acid complex and their performance in catalytic partial oxidation of methane. J Energy Chem 23 (2), 235–243. https://doi.org/10.1016/s2095-4956(14)60141-8.

Zhang, H., Wang, Z.Z., Li, S.S., et al., 2017. Correlation between structure, acidity and activity of Mo-promoted Pt/ZrO_2-TiO_2-Al_2O_3 catalysts for *n*-decane catalytic cracking. Appl. Therm. Eng. 111, 811–818. https://doi.org/10.1016/j.applthermaleng.2016.10.006.

Zhang, J., Chen, T., Jiao, Y., et al., 2020. Role of acidity in catalytic cracking of *n*-decane over supported Pt-based catalysts. Appl. Surf. Sci. 507. https://doi.org/

10.1016/j.apsusc.2019.145113.
Zhang, Z.M., Hu, X., Li, J.J., et al., 2018. Steam reforming of acetic acid over Ni/Al_2O_3 catalysts: correlation of nickel loading with properties and catalytic behaviors of the catalysts. Fuel 217, 389–403. https://doi.org/10.1016/j.fuel.2017.12.114.
Zhu, Y.H., Peng, W., Xu, R.N., et al., 2018. Review on active thermal protection and its heat transfer for airbreathing hypersonic vehicles. Chin. J. Aeronaut. 31 (10), 1929–1953. https://doi.org/10.1016/j.cja.2018.06.011.